

CrossMark  
click for updatesCite this: *J. Mater. Chem. A*, 2016, 4, 13242

# Facile one-pot solvothermal preparation of Mo-doped Bi<sub>2</sub>WO<sub>6</sub> biscuit-like microstructures for visible-light-driven photocatalytic water oxidation†

Atangana Etogo,<sup>a</sup> Ren Liu,<sup>a</sup> Jiabin Ren,<sup>a</sup> Liwen Qi,<sup>a</sup> Changcheng Zheng,<sup>b</sup> Jiqiang Ning,<sup>c</sup> Yijun Zhong<sup>a</sup> and Yong Hu<sup>\*ad</sup>

The adsorption behavior and the separation efficiency of photogenerated electron–hole pairs are two important elements in estimating the photocatalytic activity of a photocatalyst. In this work, we have developed a facile one-pot solvothermal method for the preparation of Mo-doped Bi<sub>2</sub>WO<sub>6</sub> with uniform three-dimensional (3D) hierarchical porous biscuit-like microstructures (PBMs). Mo doping is found to have two important roles in the synthesis of Bi<sub>2</sub>WO<sub>6</sub> particles, leading to porous microstructures and adjusting band gaps of the Bi<sub>2</sub>Mo<sub>x</sub>W<sub>1-x</sub>O<sub>6</sub> particles. The band structure of the as-prepared porous Bi<sub>2</sub>Mo<sub>x</sub>W<sub>1-x</sub>O<sub>6</sub> products is characterized by UV-vis diffuse reflectance spectroscopy and valence-band X-ray photoelectron spectroscopy. Density functional theory (DFT) calculations give further insights into the band structure of the Bi<sub>2</sub>Mo<sub>x</sub>W<sub>1-x</sub>O<sub>6</sub> products. In all the samples, Bi<sub>2</sub>Mo<sub>0.21</sub>W<sub>0.79</sub>O<sub>6</sub> PBMs exhibit a very efficient catalytic performance in oxidizing water under visible light irradiation ( $\lambda > 420$  nm), with an average O<sub>2</sub> evolution rate of up to 147.2  $\mu\text{mol h}^{-1} \text{g}^{-1}$  and an apparent quantum efficiency (QE) of 3.1% at 420 nm, representing a 2 times more enhancement compared with the non-doped Bi<sub>2</sub>WO<sub>6</sub> sample. This study provides a simple method for designing metal-doped semiconductors with porous structures for different applications.

Received 13th June 2016  
Accepted 27th July 2016

DOI: 10.1039/c6ta04923k

www.rsc.org/MaterialsA

## 1. Introduction

Photocatalysis has been regarded as an environmentally friendly and economical technology which is widely used in the decomposition of organic pollutants, water splitting for hydrogen production, conversion of CO<sub>2</sub> to hydrocarbon fuel, *etc.*<sup>1,2</sup> With naturally abundant water and solar light, photocatalytic water splitting provides an approach to convert solar energy directly into a renewable and storable hydrogen source.<sup>3</sup> A narrow-gap semiconductor is highly desirable to effectively use solar energy, but narrowing the band gap of a photocatalyst decreases the driving force for redox reactions. Moreover, visible-light-driven water oxidation has a fundamental scientific challenge because of the slow kinetics of water oxidation induced by a complex multielectron oxidation process and huge activation energy barrier for O–O bond formation.<sup>4–7</sup> To date,

Ru- and Ir-based oxides have been the most effective visible-light-driven water oxidation catalysts. Due to their limited availability and unacceptable cost, the development of a suitable water oxidation photocatalyst containing earth-abundant elements is desirable but challenging.<sup>8</sup>

As one of the simplest Aurivillius oxides with a layered structure, Bi<sub>2</sub>WO<sub>6</sub> is an important visible-light responsive photocatalyst with a narrow band gap of 2.8 eV, exhibiting good photocatalytic performance in degradation of organic dyes and visible-light photocatalytic evolution of oxygen.<sup>9,10</sup> However, there are several issues limiting its water oxidation application, including low electrical conductivity and instability in water, and weak energy-conversion efficiency owing to rapid recombination of photoinduced electron–hole pairs.<sup>11</sup> To overcome these obstacles, numerous attempts have been made to improve the photocatalytic activity of Bi<sub>2</sub>WO<sub>6</sub>, such as formation of porous structures to enhance the surface area,<sup>12,13</sup> combination with other semiconductors to fabricate hetero-junction nanostructures,<sup>14–16</sup> loading co-catalysts,<sup>17,18</sup> impurity doping,<sup>19–21</sup> *etc.* Impurity doping is a method to incorporate a small percentage of foreign atoms into the regular crystal lattice of semiconductors, which can produce dramatic changes in their electrical properties by increasing electron or hole densities. For example, Allen's group has reported that doping zinc to replace a small fraction of tungsten (W) into Bi<sub>2</sub>WO<sub>6</sub> could improve the photocatalytic activity for water oxidation.<sup>22</sup>

<sup>a</sup>Institute of Physical Chemistry, Zhejiang Normal University, Jinhua, 321004, P. R. China. E-mail: yonghu@zjnu.edu.cn

<sup>b</sup>Mathematics and Physics Centre, Department of Mathematical Sciences, Xi'an Jiaotong-Liverpool University, Suzhou 215123, P. R. China

<sup>c</sup>Vacuum Interconnected Nanotech Workstation, Suzhou Institute of Nano-Tech and Nano-Bionics, Chinese Academy of Sciences, Suzhou 215123, P. R. China

<sup>d</sup>State Key Lab of Silicon Materials, College of Materials Science and Engineering, Zhejiang University, Hangzhou, 310027, P. R. China

† Electronic supplementary information (ESI) available. See DOI: 10.1039/c6ta04923k

Recent studies have shown that the introduction of molybdenum (Mo) atoms into the W sites in the host lattice of  $\text{Bi}_2\text{WO}_6$  could not only decrease the band gap energy of  $\text{Bi}_2\text{WO}_6$ , but also considerably improve the photocatalytic activity for the degradation of organic pollutants.<sup>23,24</sup> Owing to different ion radii, the substitution of Mo might induce a slight modification of the  $\text{Bi}_2\text{WO}_6$  crystal structure and result in dramatic influence on the mobility of charge carriers. In particular, the optical response of  $\text{Bi}_2\text{WO}_6$  could also be changed due to the change of the d electronic configuration due to Mo introduction. Furthermore, three-dimensional (3D) microscale architectures with mesoporous structures fabricated from nanosized building blocks possess many advantages, such as abundant transport paths for small molecules, improved photocatalytic activity, and comparative ease of separation and recyclability.<sup>25–27</sup> Therefore, from the viewpoint of developing a highly efficient visible-light-driven photocatalyst, preparing a Mo-doped  $\text{Bi}_2\text{WO}_6$  photocatalyst with a 3D porous structure is a valuable strategy.

In the present work, uniform 3D  $\text{Bi}_2\text{Mo}_x\text{W}_{1-x}\text{O}_6$  ( $x = 0, 0.21, 0.35, 0.65, \text{ and } 1$ ) with hierarchical porous biscuit-like microstructures (PBMs) has been successfully prepared by a facile one-pot solvothermal method. By varying Mo content, both the microstructure and band gap of the photocatalyst can be tuned, leading to enhanced visible light photocatalytic activity for water oxidation. In all the samples, the as-prepared  $\text{Bi}_2\text{Mo}_{0.21}\text{W}_{0.79}\text{O}_6$  PBM exhibits the highest oxygen evolution rate in all the samples studied in this work. The origin of the enhanced photoactivity related to the substitution of W with Mo is systematically studied on the basis of the crystal structure and electronic structure by utilizing the methods of UV-visible diffuse reflectance spectroscopy (UV-DRS), valence-band X-ray photoelectron spectroscopy (VB-XPS), Mott–Schottky plots and density functional theory (DFT) calculations.

## 2. Experimental section

### 2.1. Synthesis of 3D $\text{Bi}_2\text{Mo}_x\text{W}_{1-x}\text{O}_6$ PBMs

All reagents are of analytical grade, purchased from the Shanghai Chemical Reagent Factory, and used as received without further purification.  $\text{Bi}_2\text{Mo}_x\text{W}_{1-x}\text{O}_6$  ( $x = 0, 0.21, 0.35, 0.65, \text{ and } 1$ ) microstructures were synthesized *via* a simple solvothermal method.  $\text{Bi}(\text{NO}_3)_3 \cdot 5\text{H}_2\text{O}$ ,  $\text{Na}_2\text{MoO}_4 \cdot 2\text{H}_2\text{O}$  and  $\text{Na}_2\text{WO}_4 \cdot 2\text{H}_2\text{O}$  were used as metal sources in stoichiometric proportions to form  $\text{Bi}_2\text{Mo}_x\text{W}_{1-x}\text{O}_6$  products. In a typical synthetic procedure, 364 mg of  $\text{Bi}(\text{NO}_3)_3 \cdot 5\text{H}_2\text{O}$  and 0.8 g of polyvinylpyrrolidone (PVP, MW  $\sim 58\text{k}$ ) were dissolved in 20 mL ethylene glycol (EG) with the assistance of ultrasonication for 15 min, followed by dropwise addition of  $\text{Na}_2\text{MoO}_4 \cdot 2\text{H}_2\text{O}$  aqueous solution (10 mL) of pre-determined concentration. After vigorous stirring for 10 min, 10 mL of  $\text{Na}_2\text{WO}_4 \cdot 2\text{H}_2\text{O}$  aqueous solution of pre-determined concentration was added drop by drop and then kept under vigorous magnetic stirring for 20 min. The resulting mixture was sealed in a 50 mL of PTFE-lined stainless steel autoclave and was heated at 180 °C for 15 h. Finally, the resulting  $\text{Bi}_2\text{Mo}_x\text{W}_{1-x}\text{O}_6$  products were collected by centrifugation, repeatedly washed with ethanol and distilled water three times, and then dried in an oven at 80 °C for 4 h. To

investigate the effect of  $\text{Na}_2\text{MoO}_4 \cdot 2\text{H}_2\text{O}$ , different concentrations of  $\text{Na}_2\text{MoO}_4 \cdot 2\text{H}_2\text{O}$  (0, 0.0375, 0.05, and 0.06 mM) and  $\text{Na}_2\text{WO}_4 \cdot 2\text{H}_2\text{O}$  (0, 0.015, 0.025, and 0.0375 mM) were stoichiometrically changed in the reactions, while other conditions remain unchanged. The resultant products were designated as  $\text{Bi}_2\text{WO}_6$ ,  $\text{Bi}_2\text{Mo}_{0.21}\text{W}_{0.79}\text{O}_6$ ,  $\text{Bi}_2\text{Mo}_{0.35}\text{W}_{0.65}\text{O}_6$ ,  $\text{Bi}_2\text{Mo}_{0.65}\text{W}_{0.35}\text{O}_6$ , and  $\text{Bi}_2\text{MoO}_6$ , respectively. The Mo content in the precursor solution was defined as  $x$ , and  $x = \text{Mo}/(\text{Mo} + \text{W})$ .

### 2.2. Characterization

Powder X-ray diffraction (XRD) measurements of the samples were performed with a Philips PW3040/60 X-ray diffractometer using  $\text{Cu K}\alpha 1$  radiation at a scanning rate of 0.06 deg  $\text{s}^{-1}$ . Scanning electron microscopy (SEM) was performed by using a Hitachi S-4800 scanning electron micro-analyzer with an accelerating voltage of 15 kV. Transmission electron microscopy (TEM) was conducted on a JEM-2100F field emission TEM. Samples for TEM measurements were prepared by dispersing the products in ethanol and placing several drops of the suspension on a holey carbon net supported on copper grids. Further evidence for the composition of the products was provided by XPS, using an ESCALab MKII X-ray photoelectron spectrometer with  $\text{Mg K}\alpha$  X-rays as the excitation source. UV-vis DRS spectra of the as-prepared samples were recorded over the range of 200–800 nm in the absorption mode employing a Thermo Nicolet Evolution 500 UV-vis spectrophotometer equipped with an integrating sphere attachment. Raman spectra were collected by using a Renishaw RM1000 confocal microscope under ambient conditions, and the wavelength of the excitation laser is 514 nm. The Mott–Schottky measurements were performed at a fixed frequency of 100 Hz with 10 mV amplitude on a Autolab PGSTAT302N station (Metrohm Autolab B.V, Holland) using a standard three-electrode cell with 0.5 M  $\text{Na}_2\text{SO}_4$ , a working electrode, a platinum wire as the counter electrode, and standard  $\text{Ag}/\text{AgCl}$  in saturated KCl as the reference electrode. Electrochemical impedance spectra (EIS) were acquired by applying an AC voltage of 10 mV amplitude in the frequency range of 0.1 Hz to 100 kHz also in a three-electrode system with a  $\text{K}_3[\text{Fe}(\text{CN})_6]$  (5 mM) and KCl (1 M) aqueous solution. The plane-wave-based DFT calculations of  $\text{Bi}_2\text{Mo}_x\text{W}_{1-x}\text{O}_6$  samples were performed with the CASTEP program package with core orbitals replaced by ultrasoft pseudopotentials, generalized gradient approximation (GGA) with the PBE exchange–correlation functional, and a kinetic energy cutoff at 420 eV. Ninety-six atom supercells were constructed, and all band structures and the density of states were calculated on the corresponding optimized crystal geometries.

### 2.3. Photocatalytic $\text{O}_2$ evolution experiments

The photocatalytic  $\text{O}_2$  evolution reactions were carried out in a water-cooled Pyrex cell using a 300 W xenon lamp (Micro-Solar300, PerfectLight) with an optical cut-on filter ( $\lambda > 420 \text{ nm}$ ). In a typical reaction, 100 mg of the catalyst was dispersed in 100 mL aqueous solution containing 0.1 M NaOH and 0.02 M  $\text{Na}_2\text{S}_2\text{O}_8$ . The reaction mixture in the cell was cooled (20 °C) by a continuous flow of water. Before irradiation, the suspension

was purged with argon for at least 90 min to drive off the air inside. 5%  $\text{Co}_3\text{O}_4$  was loaded on the surface of the as-prepared photocatalysts, and the analysis of the  $\text{O}_2$  evolution was performed using an online gas chromatograph (Agilent Technologies GC-7890B, TCD, He carrier).

### 3. Results and discussion

The XRD patterns of the as-prepared 3D  $\text{Bi}_2\text{Mo}_x\text{W}_{1-x}\text{O}_6$  microstructures with different concentrations of metal precursors (W and Mo) are shown in Fig. S1 (see ESI†). For pure  $\text{Bi}_2\text{WO}_6$  and  $\text{Bi}_2\text{Mo}_x\text{W}_{1-x}\text{O}_6$  microstructures with different concentrations of Mo, all the diffraction peaks can be well indexed to the orthorhombic  $\text{Bi}_2\text{WO}_6$  phase (JCPDS no. 39-0256,  $a = 5.457 \text{ \AA}$ ,  $b = 16.435 \text{ \AA}$  and  $c = 5.438 \text{ \AA}$ ), which illustrates that Mo-substitution did not result in the development of new crystal orientations or changes in preferential orientations. The similarity of the diffractograms suggests that these compounds are isostructural with a pure orthorhombic  $\text{Bi}_2\text{WO}_6$  phase. However, with the increase of Mo content, the (131) diffraction peak in the range of  $2\theta = 27\text{--}30^\circ$  (Fig. 1a) demonstrates a remarkable shift toward a larger  $2\theta$  value. According to Bragg's law (eqn (1)),

$$d_{(hkl)} = \frac{n\lambda}{2 \sin \theta} \quad (1)$$

where  $d_{(hkl)}$  is the distance between crystal planes of  $(h \ k \ l)$ ,  $\lambda$  is the X-ray wavelength, and  $\theta$  is the diffraction angle of the crystal plane  $(h \ k \ l)$ , the increase in the  $2\theta$  value should result from the shrinkage of the lattice parameters  $d_{(113)}$ . The ionic radius of Mo (134.2 pm) is smaller than that of W (137 pm), and the substitution of  $\text{W}^{6+}$  by  $\text{Mo}^{6+}$  would result in a decrease of the  $d_{(hkl)}$  value and thus an increase of the  $2\theta$  values. Therefore, the observed shift of the diffraction peak toward a higher angle may be caused by the substitution of  $\text{W}^{6+}$  by  $\text{Mo}^{6+}$ .<sup>28</sup> Furthermore, it can be seen that the amplified  $2\theta$  peak around  $28^\circ$  for all the  $\text{Bi}_2\text{Mo}_x\text{W}_{1-x}\text{O}_6$  samples only consists of a single XRD peak, rather than the mixture of the two respective peaks of  $\text{Bi}_2\text{MoO}_6$  and  $\text{Bi}_2\text{WO}_6$ , indicating that the as-prepared products can be referred to as solid solutions.<sup>29</sup> To examine the effect of  $\text{Mo}^{6+}$  incorporation into the  $\text{Bi}_2\text{WO}_6$  host matrix, the evolution of the lattice parameters was investigated by the DFT calculations. The determined lattice parameters are shown in Table S1 (see ESI†),

indicating a regular increase of  $a$  and  $b$  (cell constants) with the increase of Mo content. In addition to lattice expansion, an increase in the  $\gamma$  angle was also observed (Fig. S2, see ESI†), which indicates the lowered symmetry at high dopant concentration. These observations confirm the direct substitution of  $\text{Mo}^{6+}$  for the  $\text{W}^{6+}$  in  $\text{Bi}_2\text{WO}_6$ .<sup>30,31</sup>

Raman spectra of the  $\text{Bi}_2\text{Mo}_x\text{W}_{1-x}\text{O}_6$  samples are shown in Fig. 1b. In general, all Raman bands for  $\text{Bi}_2\text{WO}_6$  above  $400 \text{ cm}^{-1}$  were assigned to W–O stretching modes and assumed to directly measure W–O bond lengths in W species.<sup>32</sup> In more detail, the bands at  $795$  and  $825 \text{ cm}^{-1}$  were associated with antisymmetric and symmetric  $A_g$  modes of the  $\text{WO}_6$  octahedra that involve motions of the apical oxygen atoms that are perpendicular to the layers.<sup>33</sup> Raman bands observed in the range of  $600\text{--}1000 \text{ cm}^{-1}$  for  $\text{Bi}_2\text{MoO}_6$  can be assigned to Mo–O stretches, and those below  $400 \text{ cm}^{-1}$  belong to bending, wagging, and external modes of Mo–O bonds.<sup>34</sup> A strong band at  $795 \text{ cm}^{-1}$  along with two shoulder bands at  $843$  and  $712 \text{ cm}^{-1}$  of  $\text{Bi}_2\text{MoO}_6$  is observed, corresponding to Mo–O stretching modes of the distorted  $\text{MoO}_6$  octahedra. In the  $\text{Bi}_2\text{Mo}_x\text{W}_{1-x}\text{O}_6$  samples, it is notable that the band at  $825 \text{ cm}^{-1}$  is shifted to higher wavenumbers with increasing Mo content, which might be attributed to different metal–oxygen bond lengths within  $\text{WO}_6$  and  $\text{MoO}_6$  octahedra related to the apical oxygen atoms, indicating a decrease of the apical W–O bond length. This could be explained by the fact that the Bi–O–W bonds could be partially displaced by Bi–O–Mo *via*  $\text{Mo}^{6+}$  doping. Similar results were also reported in Li group's work.<sup>35</sup> On the other hand, the mode at  $712 \text{ cm}^{-1}$  exhibits no evident shift and broadening.

To explore the chemical environment surrounding the W and Bi elements in  $\text{Bi}_2\text{Mo}_x\text{W}_{1-x}\text{O}_6$  samples, the as-prepared 3D  $\text{Bi}_2\text{Mo}_{0.21}\text{W}_{0.79}\text{O}_6$  PBM was characterized by XPS in detail, as shown in Fig. S3 (see ESI†). The survey spectrum (Fig. S3a†) reveals that the sample contains only O, Bi, W and Mo elements. Fig. S3b† shows the high-resolution XPS spectrum of O 1s located at  $529.11 \text{ eV}$ . Fig. S3c† displays the high-resolution XPS spectrum of Bi 4f; two symmetric peaks are located at  $158.37$  and  $163.70 \text{ eV}$  which can be attributed to Bi 4f<sub>7/2</sub> and Bi 4f<sub>5/2</sub> lines, respectively, and the peaks at  $37.6.0$  and  $35.5 \text{ eV}$  in Fig. S3d† correspond to W 4f<sub>5/2</sub> and W 4f<sub>7/2</sub>, respectively, both of which can be assigned to the  $\text{W}^{6+}$  oxidation state.<sup>36</sup> As shown in Fig. S3e,† the Mo 3d<sub>3/2</sub> and Mo 3d<sub>5/2</sub> peaks located at  $235.6$  and

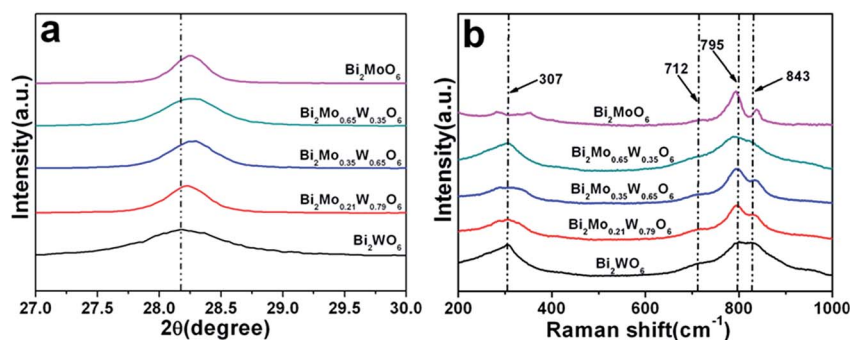


Fig. 1 (a) XRD patterns of the as-prepared  $\text{Bi}_2\text{Mo}_x\text{W}_{1-x}\text{O}_6$  composites in the range of  $27\text{--}30^\circ$  and (b) Raman spectra of  $\text{Bi}_2\text{WO}_6$ ,  $\text{Bi}_2\text{MoO}_6$  and Mo-doped  $\text{Bi}_2\text{WO}_6$  samples.

232.4 eV, respectively, imply that the chemical state of Mo in the  $\text{Bi}_2\text{Mo}_{0.21}\text{W}_{0.79}\text{O}_6$  system is +6.<sup>37</sup> The energy difference between the two peaks is 3.2 eV, suggesting that Mo cations are mainly  $\text{Mo}^{6+}$  in the site of  $\text{W}^{6+}$  in  $\text{Bi}_2\text{WO}_6$ . This result is in good agreement with that of previously reported Mo-doped metal oxides.<sup>38,39</sup>

The morphology and structure of the as-obtained samples were characterized by SEM. Fig. S4a (see ESI†) shows the low-magnification SEM image of the  $\text{Bi}_2\text{WO}_6$ , indicating that the products are flower-like structures with average diameters ranging from 2 to 3  $\mu\text{m}$ . Additionally, it can be seen that the flower-like microstructures are constructed by nanosheets about 15 nm thick. The low-magnification SEM image of the  $\text{Bi}_2\text{MoO}_6$  sample exhibits plate-like structures about 100 nm, as displayed in Fig. S4b (see ESI†). A panoramic SEM image of the as-prepared  $\text{Bi}_2\text{Mo}_{0.21}\text{W}_{0.79}\text{O}_6$  PBMs is shown in Fig. 2a, indicating that the product bears a strong resemblance to the morphology of hierarchical porous biscuit-like microstructures with a nearly uniform size of *ca.* 2.1  $\mu\text{m}$  in diameter. The magnified SEM image of an individual biscuit-like structure (Fig. 2b) further reveals that the microstructure consists of building blocks of individual nanoparticles. As can be seen in the  $\text{Bi}_2\text{Mo}_{0.35}\text{W}_{0.65}\text{O}_6$  microstructure (Fig. S4c and d†), upon higher Mo contents, these nanoparticle building blocks further assemble into building blocks at the surface of the biscuit-like microstructures. Hence, the as-obtained microstructure may be seeded at the centre and grow peripheral *via* oriented attachment of the building blocks. These hierarchical biscuit-like microstructures start to disintegrate upon further

increase of Mo contents, as shown in the  $\text{Bi}_2\text{Mo}_{0.65}\text{W}_{0.35}\text{O}_6$  material (Fig. S4e and f†), and this process continues until the building blocks self-aggregate into individual nanodisks. The morphology of  $\text{Bi}_2\text{MoO}_6$  is similar to that of  $\text{Bi}_2\text{Mo}_{0.65}\text{Mo}_{0.35}\text{O}_6$ , and their particle size is about 100 nm. It is worth pointing out that, for almost all nanocrystals, dopants and their relevant defects can be expelled from the internal bulk lattice to surfaces by a “self-purification” process.<sup>40,41</sup> The nanoparticles have a tendency to segregate out the dopant or impurity atoms towards the surface, leading to a greater dopant concentration near the cover than that at the interior.<sup>42,43</sup> We believe that this process may lead to alteration of the nanocrystal surface, morphology and particle sizes. This could also explain the mesoporous structure on the surface of  $\text{Bi}_2\text{Mo}_{0.21}\text{W}_{0.79}\text{O}_6$  PBMs. The porous structure of  $\text{Bi}_2\text{Mo}_{0.21}\text{W}_{0.79}\text{O}_6$  PBMs is further revealed by the TEM image, as shown in Fig. 2c, revealing that the biscuit-like microstructures consist of individual nanoparticles, building blocks with a thickness of about 20 nm and the mesoporous surface is uniform. The HRTEM image in Fig. 2d shows a lattice fringe in the  $\text{Bi}_2\text{Mo}_{0.21}\text{W}_{0.79}\text{O}_6$  PBM. The interplanar spacing is about 0.272 nm, corresponding to the (002) plane of the pure orthorhombic  $\text{Bi}_2\text{WO}_6$  phase. The elemental mapping analysis results shown in Fig. 2e–h reveal that the  $\text{Bi}_2\text{Mo}_{0.21}\text{W}_{0.79}\text{O}_6$  PBM product is composed of Bi, O, W and Mo elements which are uniformly distributed throughout the entire  $\text{Bi}_2\text{Mo}_{0.21}\text{W}_{0.79}\text{O}_6$  PBM.

To understand the growth mechanism of the  $\text{Bi}_2\text{Mo}_{0.21}\text{W}_{0.79}\text{O}_6$  PBMs, the products obtained with a series of reaction times were investigated. Fig. S5a (see ESI†) shows the product obtained by continuously stirring the precursor at room temperature for 20 min, indicating the formation of tiny nuclei. When the precursor was solvothermally treated for 1.5 h at 180 °C, the product was amorphous nanoparticles without a discernible morphology (Fig. S5b, see ESI†). As the reaction was prolonged to 5 h, multilayered biscuit-like microstructures made of nanoparticle building blocks became the predominant product (Fig. S5c, see ESI†). Longer reaction time led to the formation of large (2–2.1  $\mu\text{m}$ ) biscuit-like microstructures. The particle size was not greatly changed when the reaction time was longer than 10 h (Fig. S5d, see ESI†), and well-assembled biscuit-like architectures constructed by numerous nanoparticle building blocks were formed when the reaction lasted for 15 h. But at a low temperature of 90 °C in a water bath for 15 h, the product was still tiny nanoparticles as shown in Fig. S5e and f (see ESI†). The influence of the solvent was also investigated by studying the products obtained at 180 °C. When only water was employed as the solvent, non-uniform heterostructured sheet-like microstructures were obtained, as shown in Fig. S6a (see ESI†). When EG was used as the solvent, only some irregular nanospheres were obtained (Fig. S6b, see ESI†). These results clearly suggest that the use of a mixed solvent (EG/water) is primordial for the growth of multilayered biscuit-like microstructures.

Based on the aforementioned SEM observations, the formation mechanism of the multilayered biscuit-like microstructures can be explained. Initially, when PVP is added into

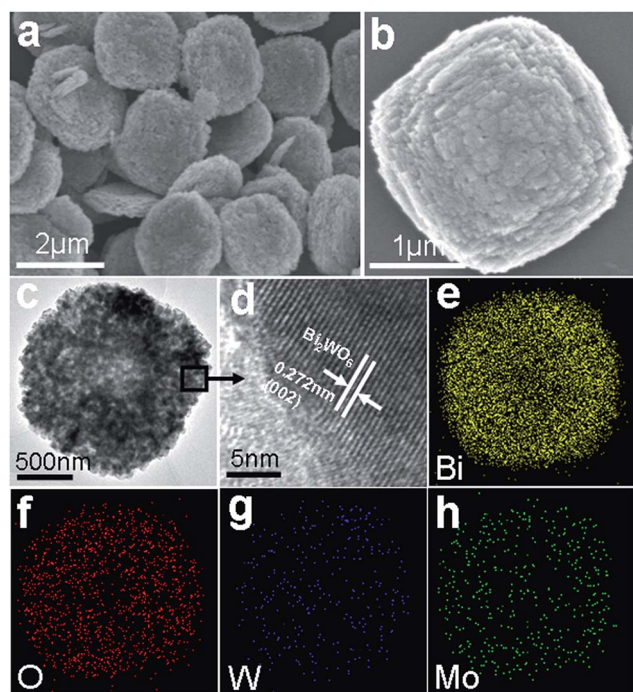


Fig. 2 (a) and (b) SEM images of the as-prepared  $\text{Bi}_2\text{Mo}_{0.21}\text{W}_{0.79}\text{O}_6$  PBMs; (c) TEM image and (d) HRTEM image and (e) Bi, (f) O, (g) W and (h) Mo elemental mapping images of the  $\text{Bi}_2\text{Mo}_{0.21}\text{W}_{0.79}\text{O}_6$  PBM sample.

$\text{Bi}(\text{NO}_3)_3 \cdot 5\text{H}_2\text{O}$  solution, an intermediate complex of  $\text{Bi}^{3+}$ -PVP can be formed to decrease the concentration of free  $\text{Bi}^{3+}$  in solution, which results in a relatively slow reaction rate and thus facilitates the growth of high-quality crystals in view of the kinetic process. When W and Mo ions are introduced,  $\text{Bi}^{3+}$ -PVP may compete with  $\text{WO}_4^{2-}$  and  $\text{MoO}_4^{2-}$  for  $\text{Bi}^{3+}$ . When  $\text{WO}_4^{2-}$  and  $\text{MoO}_4^{2-}$  coordinate with  $\text{Bi}^{3+}$ ,  $\text{Bi}_2\text{Mo}_x\text{W}_{1-x}\text{O}_6$  is formed. It is plausible that in the early stage  $\text{Bi}^{3+}$  and  $\text{WO}_4^{2-}$  ions would form a  $\text{Bi}_2\text{WO}_6$  crystal nucleus and the grain growth would eventually occur and at high temperature  $\text{Mo}^{6+}$  ions can readily substitute  $\text{W}^{6+}$  in the  $\text{Bi}_2\text{WO}_6$  leading to the formation of  $\text{Bi}_2\text{Mo}_x\text{W}_{1-x}\text{O}_6$  nanoparticles. Thus, tiny  $\text{Bi}_2\text{Mo}_x\text{W}_{1-x}\text{O}_6$  nuclei are generated in the supersaturated solution, and the size of the nanoparticles increases over time. The bigger particles grow at the expense of the smaller ones, because there is a solubility difference between relatively larger and smaller particles according to the well-known Gibbs–Thomson law.<sup>44</sup> The introduced  $\text{Mo}^{6+}$  dopants and their relevant defects can be expelled from the internal bulk lattice to surfaces by a “self-purification” process, leading to the alteration of the nanocrystal surface, morphology and particle sizes. For long reaction time, the nanoparticles self-assemble into multi-layered building blocks through the Ostwald ripening process and create porous biscuit-like microstructures *via* peripheral growth. As a result of self-assembly of the building blocks, the resultant  $\text{Bi}_2\text{Mo}_{0.21}\text{W}_{0.79}\text{O}_6$  PBMs possess mesoporous structures.

The nitrogen adsorption–desorption isotherms are employed to characterize the porous structure of the  $\text{Bi}_2\text{Mo}_{0.21}\text{W}_{0.79}\text{O}_6$  PBMs, and the corresponding pore size distribution curves obtained by the BJH method are shown in Fig. S7 (see ESI†). The sample exhibits typical IV characteristics with an obvious capillary condensation step, indicating the presence of a pronounced inter-particle mesopore size distribution,<sup>45</sup> exhibiting a specific surface area of  $12.89 \text{ m}^2 \text{ g}^{-1}$  with an average pore size of 27.54 nm. Additionally, the specific surface areas of samples  $\text{Bi}_2\text{Mo}_{0.35}\text{W}_{0.65}\text{O}_6$ ,  $\text{Bi}_2\text{Mo}_{0.65}\text{W}_{0.35}\text{O}_6$ ,  $\text{Bi}_2\text{WO}_6$  and  $\text{Bi}_2\text{MoO}_6$  are 13.2, 12.4, 11.1 and  $11.2 \text{ m}^2 \text{ g}^{-1}$ , respectively. Therefore, this result indicates that the surface area is not the determining factor for photocatalytic  $\text{O}_2$  evolution in this case. Fig. 3a shows the UV-DRS spectra of the  $\text{Bi}_2\text{Mo}_x\text{W}_{1-x}\text{O}_6$  samples, where the spectra exhibit a steep-edged profile, indicating the visible light absorption due to the band gap

transition.<sup>46</sup> The band-gap energies of all the samples were estimated from the absorption spectra by using the following relationship:

$$\alpha h\nu = A(h\nu - E_g)^{n/2} \quad (2)$$

where  $\alpha$ ,  $h\nu$  and  $E_g$  are the absorption coefficient, photon energy, and the band gap energy, respectively, and  $A$  is a constant. The value of  $n$  for  $\text{Bi}_2\text{WO}_6$  is 2, which means that the corresponding optical transition is indirect.<sup>47</sup> The absorption edge of  $\text{Bi}_2\text{Mo}_x\text{W}_{1-x}\text{O}_6$  shifts toward lower energy as the value of  $x$  increased. The band gap energies estimated from eqn (2) are 2.96, 2.43, 2.52, 2.47, and 2.56 eV, for  $\text{Bi}_2\text{Mo}_x\text{W}_{1-x}\text{O}_6$  with  $x = 0, 0.21, 0.35, 0.65,$  and 1, respectively (Fig. 3b), indicating a strong influence of Mo concentration on the optical properties and band structure of the as-prepared  $\text{Bi}_2\text{Mo}_x\text{W}_{1-x}\text{O}_6$  catalysts. It is noteworthy that the onset of the diffuse reflectance spectra with Mo substitution is not linearly shifted. The overall band gap of a given  $\text{Bi}_2\text{Mo}_x\text{W}_{1-x}\text{O}_6$  compound can be thought to depend mainly on two factors: (i) the degree of Mo 4d and W 5d orbitals being involved in the conduction band (CB) of  $\text{Bi}_2\text{Mo}_x\text{W}_{1-x}\text{O}_6$  and (ii) the degree of delocalization of excitation energy due to the distortion of the crystal structure arising from Mo substitution.<sup>48</sup>

To examine the electronic structure modification of  $\text{Bi}_2\text{WO}_6$  by substitutional dopants, the density of states (DOS) is calculated by DFT calculations. Fig. S8 (see ESI†) shows the projected partial density of states of the  $\text{Bi}_2\text{WO}_6$  and  $\text{Bi}_2\text{Mo}_x\text{W}_{1-x}\text{O}_6$  ( $x = 0.25, 0.5,$  and 0.75) samples. The band gap energy of pure  $\text{Bi}_2\text{WO}_6$  is 2.29 eV, which is smaller than the experimental value of 2.96 eV due to the well-known shortcoming of the exchange-correction functional in describing excited states.<sup>49</sup> The band calculation results show that  $\text{Bi}_2\text{Mo}_x\text{W}_{1-x}\text{O}_6$  ( $x = 0.25, 0.5,$  and 0.75) samples have direct band gaps. The calculated band gaps are about 2.239, 2.247, and 2.234 eV, with the increase of Mo doping (for  $x = 0.25, 0.5,$  and 0.75), respectively. The DOS of pure  $\text{Bi}_2\text{WO}_6$  displays that the VB is mainly composed of O 2p, Bi 6s, Bi 6p and small W 5d states, while the CB is formed dominantly by W 5d, Bi 6p and small O 2p states, as displayed in Fig. S8a (see ESI†). It is revealed that the visible-light response for  $\text{Bi}_2\text{WO}_6$  is due to the transition from the hybridized Bi 6s and O 2p states in the VB to W 5d states in the CB.<sup>50</sup> In the case

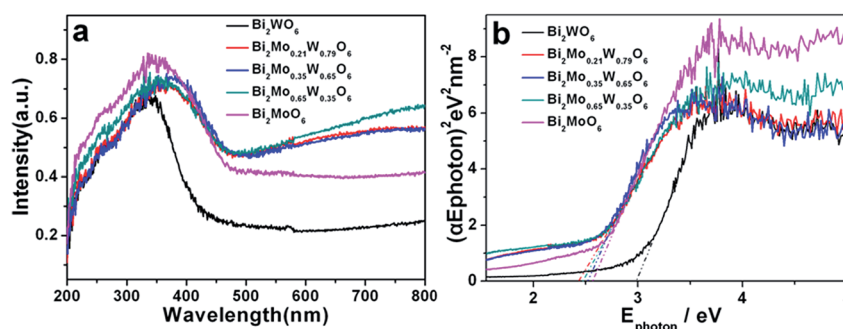


Fig. 3 (a) UV-vis diffuse reflectance spectra of  $\text{Bi}_2\text{WO}_6$ ,  $\text{Bi}_2\text{MoO}_6$  and Mo-doped  $\text{Bi}_2\text{WO}_6$  samples; (b) Tauc plots of  $\text{Bi}_2\text{WO}_6$ ,  $\text{Bi}_2\text{MoO}_6$  and Mo-doped  $\text{Bi}_2\text{WO}_6$  samples.

of  $\text{Bi}_2\text{Mo}_x\text{W}_{1-x}\text{O}_6$  ( $x = 0.25, 0.5, \text{ and } 0.75$ ) samples, Fig. S8b-d† show that some new band edge levels comprised of hybridized states of Mo 4d and W 5d are introduced at the bottom of the CB for  $x = 0.25, 0.5, \text{ and } 0.75$ . The substitution of Mo mainly influences the CB edge, because Mo has the same valence electrons and close electronegativity as W and Mo 4d orbital energy is lower than W 5d orbital energy. The hybridization of Bi 6s and O 2p states makes the VB largely dispersed, which favors the mobility of photoexcited electron-hole pairs and thus facilitates a high photocatalytic efficiency.

For a better understanding of band structures of the Mo-doped  $\text{Bi}_2\text{WO}_6$  samples, Mott-Schottky and VB-XPS analyses were also performed. In the Schottky plots (Fig. 4), the flat-band potential of  $\text{Bi}_2\text{Mo}_x\text{W}_{1-x}\text{O}_6$  and  $\text{Bi}_2\text{WO}_6$  was obtained by the extrapolation of the Mott-Schottky plots. The CB potentials of  $\text{Bi}_2\text{WO}_6$  and  $\text{Bi}_2\text{Mo}_{0.21}\text{W}_{0.79}\text{O}_6$  PBMs are located at 0.22 and 0.05 eV, respectively. An obvious shift of 0.17 eV is observed for the  $\text{Bi}_2\text{Mo}_{0.21}\text{W}_{0.79}\text{O}_6$  PBM compared with the spectrum of bare  $\text{Bi}_2\text{WO}_6$ , which could be attributed to the Mo doping. Combined with the UV-Vis DRS results, the optical VB potentials of  $\text{Bi}_2\text{WO}_6$  and  $\text{Bi}_2\text{Mo}_{0.21}\text{W}_{0.79}\text{O}_6$  PBM are located at 3.18 and 2.50 eV, respectively. The VB and CB potentials of  $\text{Bi}_2\text{Mo}_{0.35}\text{W}_{0.65}\text{O}_6$  and  $\text{Bi}_2\text{Mo}_{0.65}\text{W}_{0.35}\text{O}_6$  samples are also calculated, exhibiting CB and VB potential alteration upon Mo doping, ranging from 0.22 and 3.18 eV to 0.51 and 2.50 eV, respectively, by tuning the Mo concentration.

Fig. 5 shows the VB-XPS spectra of the as-prepared  $\text{Bi}_2\text{Mo}_x\text{W}_{1-x}\text{O}_6$  ( $x = 0, 0.21, 0.35, \text{ and } 0.65$ ) samples, which display similar VB maxima and widths. Compared with bare  $\text{Bi}_2\text{WO}_6$ , the  $\text{Bi}_2\text{Mo}_{0.21}\text{W}_{0.79}\text{O}_6$  PBM shows a downshift of  $\sim 0.05$  eV of the VB maximum as well as a widened VB. This downshift is less large than the band-gap narrowing value determined by the UV-vis DRS data ( $\sim 0.53$  eV), which indicates that the CB minimum

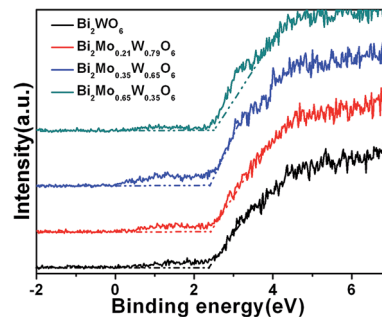


Fig. 5 VB-XPS of  $\text{Bi}_2\text{WO}_6$  (black line), and Mo-doped  $\text{Bi}_2\text{WO}_6$  (red line for  $\text{Bi}_2\text{Mo}_{0.21}\text{W}_{0.79}\text{O}_6$ , blue line for  $\text{Bi}_2\text{Mo}_{0.35}\text{W}_{0.65}\text{O}_6$  and green line for  $\text{Bi}_2\text{Mo}_{0.65}\text{W}_{0.35}\text{O}_6$ ).

of  $\text{Bi}_2\text{Mo}_{0.21}\text{W}_{0.79}\text{O}_6$  PBMs is reduced by  $\sim 0.59$  eV when compared with that of  $\text{Bi}_2\text{WO}_6$ . Table 1 shows the relative VB and CB of all the samples calculated on the basis of VB-XPS and Mott-Schottky plots. It is very clear that Mo doping into  $\text{Bi}_2\text{WO}_6$  can simultaneously induce an upward shift in the VB and

Table 1 Relative VB and CB of all the photocatalysts calculated on the basis of Mott-Schottky and VB-XPS plots

Photocatalysts	Band-gap (eV)	Mott-Schottky		VB-XPS	
		VB (eV)	CB (eV)	VB (eV)	CB (eV)
$\text{Bi}_2\text{WO}_6$	2.96	3.18	0.22	2.37	-0.59
$\text{Bi}_2\text{Mo}_{0.21}\text{W}_{0.79}\text{O}_6$	2.43	2.50	0.05	2.43	0.00
$\text{Bi}_2\text{Mo}_{0.35}\text{W}_{0.65}\text{O}_6$	2.52	2.87	0.47	2.40	-0.12
$\text{Bi}_2\text{Mo}_{0.65}\text{W}_{0.35}\text{O}_6$	2.47	3.03	0.51	2.52	0.05

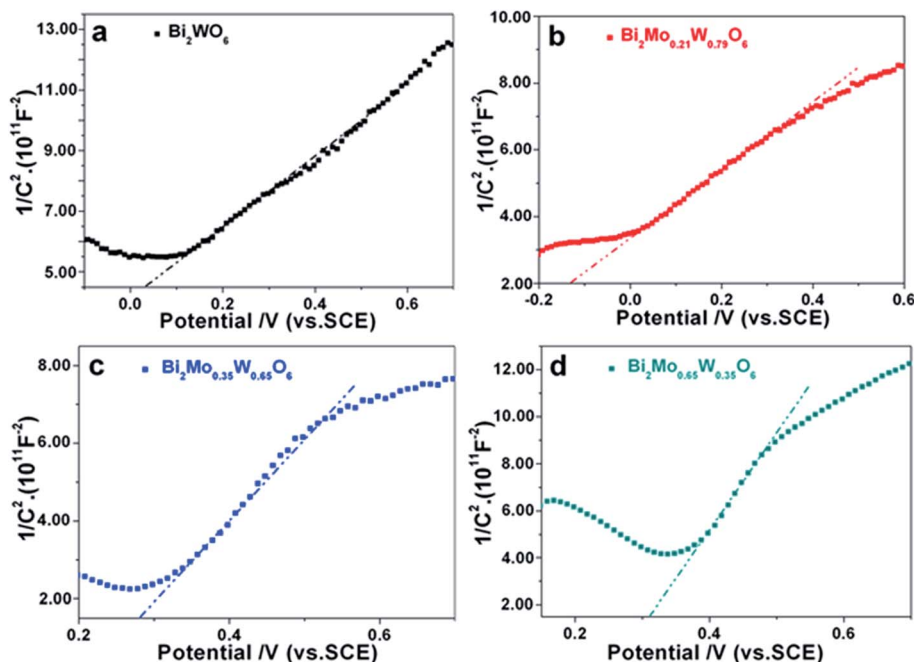
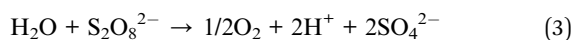


Fig. 4 Mott-Schottky plots of the (a)  $\text{Bi}_2\text{WO}_6$ , (b)  $\text{Bi}_2\text{Mo}_{0.21}\text{W}_{0.79}\text{O}_6$  (c)  $\text{Bi}_2\text{Mo}_{0.35}\text{W}_{0.65}\text{O}_6$  and (d)  $\text{Bi}_2\text{Mo}_{0.65}\text{W}_{0.35}\text{O}_6$  samples.

a downward shift in the CB, resulting in the band-gap narrowing of  $\text{Bi}_2\text{WO}_6$ . The band-gap narrowing of  $\text{Bi}_2\text{WO}_6$  upon Mo doping is attributed to creation of defect levels just below the CB of  $\text{Bi}_2\text{WO}_6$ .<sup>51</sup>

To facilitate the oxidation of water by photoexcited electrons and holes, the band gap should match the  $\text{H}_2\text{O}$  redox potential. In particular, the CB edge should be more negative than the reduction potential of  $\text{H}^+/\text{H}_2$  [0 V *versus* normal hydrogen electrode (NHE)], whereas the top of the VB should be more positive than the oxidation potential of  $\text{O}_2/\text{H}_2\text{O}$  [1.23 V].<sup>52</sup> According to the specific band gap construction, the  $\text{Bi}_2\text{Mo}_{0.21}\text{W}_{0.79}\text{O}_6$  PBM is not a good photocatalyst for hydrogen generation since its conduction band does not meet the requirements to reduce water. It should be a good choice for water oxidation to oxygen under visible-light irradiation. To characterize the catalytic performance of the as-synthesized  $\text{Bi}_2\text{Mo}_x\text{W}_{1-x}\text{O}_6$  samples, photocatalytic water oxidation tests were carried out under visible-light irradiation ( $\lambda > 420$  nm) of an aqueous solution containing  $\text{S}_2\text{O}_8^{2-}$  ions as electron acceptors. The overall photocatalytic reaction is given by eqn (3):



The oxygen evolution rates in Fig. 6a indicate that the  $\text{Bi}_2\text{Mo}_{0.21}\text{W}_{0.79}\text{O}_6$  PBM sample is a very efficient catalyst to oxidize water in the presence of 5% wt  $\text{Co}_3\text{O}_4$  nanoparticles, affording an average  $\text{O}_2$  evolution rate of  $147.2 \mu\text{mol h}^{-1} \text{g}^{-1}$ . This oxygen evolution rate represents almost a 2-fold more improvement compared to that of bare  $\text{Bi}_2\text{WO}_6$  ( $61.1 \mu\text{mol h}^{-1} \text{g}^{-1}$ ) and  $\text{Bi}_2\text{MoO}_6$  ( $62.8 \mu\text{mol h}^{-1} \text{g}^{-1}$ ). Note that there is no  $\text{O}_2$  evolution detected when the reaction is conducted in the dark or without a catalyst or  $\text{Na}_2\text{S}_2\text{O}_8$ . The apparent quantum efficiency (QE) of the  $\text{Bi}_2\text{Mo}_{0.21}\text{W}_{0.79}\text{O}_6$  sample at different wavelengths using the following eqn (4):<sup>53,54</sup>

$$\text{QE} [\%] = \frac{\text{the number of evolved } \text{O}_2 \text{ molecules} \times 4}{\text{the number of incident photons}} \times 100\% \quad (4)$$

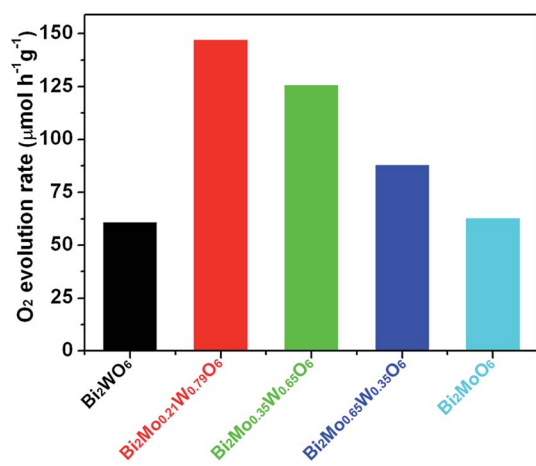


Fig. 6 Oxygen evolution rates of the as-prepared  $\text{Bi}_2\text{WO}_6$ ,  $\text{Bi}_2\text{Mo}_{0.21}\text{W}_{0.79}\text{O}_6$ ,  $\text{Bi}_2\text{Mo}_{0.35}\text{W}_{0.65}\text{O}_6$ ,  $\text{Bi}_2\text{Mo}_{0.65}\text{W}_{0.35}\text{O}_6$  and  $\text{Bi}_2\text{MoO}_6$  samples (all samples with 5% wt deposited  $\text{Co}_3\text{O}_4$ ) under visible-light irradiation.

For the  $\text{Bi}_2\text{Mo}_{0.21}\text{W}_{0.79}\text{O}_6$  sample, the apparent QE values are 3.1%, 2.5%, and 1.8% at 420, 450 and 500 nm, respectively, representing that the value decreased gradually as the incident light wavelength increased. However, the apparent QE at 420 nm of pristine  $\text{Bi}_2\text{WO}_6$  is measured to be 1.2%, indicating almost 3 fold enhancement after Mo doping (see ESI†). To rule out the heat driven  $\text{O}_2$  evolution, a series of experiments were carried out at 40 °C and 60 °C by using a precision bath circulator (Tianheng, THD-05) without visible-light irradiation, respectively. As can be seen in Fig. S9 (see ESI†), no  $\text{O}_2$  was produced after 6 h at 40 °C or 60 °C. This result demonstrates that the  $\text{O}_2$  can only be generated under visible-light irradiation.

The greatly improved oxygen evolution rate of the  $\text{Bi}_2\text{Mo}_{0.21}\text{W}_{0.79}\text{O}_6$  PBM sample could be attributed to the narrowed band-gap, and a suitable amount of Mo doping which allows a better charge separation efficiency. The repeat photocatalytic oxygen evolution and standard deviations from water splitting using the different samples as photocatalysts are shown in Fig. S10 (see ESI†). The amount of oxygen evolved increased almost linearly with time, demonstrating that the present catalyst has good repeated catalytic performance and maintains a strong driving force for water oxidation over the examined period. The activity is in an order of  $\text{Bi}_2\text{WO}_6 < \text{Bi}_2\text{MoO}_6 < \text{Bi}_2\text{Mo}_{0.65}\text{W}_{0.35}\text{O}_6 < \text{Bi}_2\text{Mo}_{0.35}\text{W}_{0.65}\text{O}_6 < \text{Bi}_2\text{Mo}_{0.21}\text{W}_{0.79}\text{O}_6$ . It should also be noted that the photocatalytic activities of the  $\text{Bi}_2\text{Mo}_x\text{W}_{1-x}\text{O}_6$  samples are much higher than those of bare  $\text{Bi}_2\text{WO}_6$  and  $\text{Bi}_2\text{MoO}_6$ .

To the best of our knowledge, this is the first report on the photocatalytic water oxidation behavior of the  $\text{Bi}_2\text{Mo}_x\text{W}_{1-x}\text{O}_6$  catalysts. Fig. S11 (see ESI†) shows a schematic overview of the present photocatalytic water oxidation reaction. Because of the electron-scavenging properties of  $\text{Na}_2\text{S}_2\text{O}_8$ ,<sup>55</sup> it is postulated that the spatial separation of photogenerated electrons and holes at  $\text{Bi}_2\text{Mo}_{0.21}\text{W}_{0.79}\text{O}_6$  PBMs through the potential gradient of  $\text{Co}_3\text{O}_4$ - $\text{Bi}_2\text{Mo}_{0.21}\text{W}_{0.79}\text{O}_6$  junctions is responsible for the higher photocatalytic activity. During the photocatalytic reaction, electrons and holes are generated by photoexcitation. The photogenerated electrons can be scavenged by  $\text{Na}_2\text{S}_2\text{O}_8$  and holes can be further transferred to the  $\text{Co}_3\text{O}_4$  co-catalyst for catalytic reactions at the surface. It should be pointed out that the  $\text{Co}_3\text{O}_4$  species can be oxidized by the photoexcited holes from the photocatalyst during the reaction because holes were trapped by the catalyst first and then took part in the following redox reaction, leading to a better charge-separation.<sup>56</sup> Table S2† summarizes the oxygen evolution rates and final moles of oxygen of all the as-prepared samples produced from the photocatalytic reactions. It is known that defect sites can be introduced into  $\text{Bi}_2\text{WO}_6$  by element doping. A suitable amount of defect sites is good for the separation of photo-generated electron-hole pairs *via* trapping effects. This could explain the superior photoactivity of  $\text{Bi}_2\text{Mo}_{0.21}\text{W}_{0.79}\text{O}_6$  PBMs. However, excess defects will become the new recombination centers for photo-generated electron-hole pairs. As a result, upon higher doping the  $\text{O}_2$  evolution rate will be considerably reduced. From Fig. S12 (see ESI†), we could also see that the EIS Nyquist plot of the as-obtained  $\text{Bi}_2\text{Mo}_{0.21}\text{W}_{0.79}\text{O}_6$  PBMs exhibits a smaller circular radius than that of other samples. This result suggests

that the charge-transfer resistance of the  $\text{Bi}_2\text{Mo}_{0.21}\text{W}_{0.79}\text{O}_6$  PBM is smaller than that of other samples.<sup>57</sup> Therefore, we can infer from the EIS Nyquist plot that efficient charge separation and better electron transport properties can be achieved with the  $\text{Bi}_2\text{Mo}_{0.21}\text{W}_{0.79}\text{O}_6$  PBMs. Furthermore, the photocurrent transient response measurements of the as-prepared products were also carried out in a 0.1 M  $\text{Na}_2\text{SO}_4$  solution under visible-light irradiation. Fig. S13 (see ESI†) displays the rapid and consistent photocurrent responses for each switch-on and -off event in multiple 40 s on-off cycles. It is worth noting that the photocurrent density of the  $\text{Bi}_2\text{Mo}_{0.21}\text{W}_{0.79}\text{O}_6$  PBM electrode is higher than that of the other samples, indicating that the  $\text{Bi}_2\text{Mo}_{0.21}\text{W}_{0.79}\text{O}_6$  PBMs possess a higher separation efficiency for the photo-induced electron-hole pairs. In this case, the  $\text{Bi}_2\text{Mo}_{0.21}\text{W}_{0.79}\text{O}_6$  PBMs reported here have great implication potential for photocatalytic water oxidation.

## 4. Conclusions

In summary, we have demonstrated the synthesis of 3D  $\text{Bi}_2\text{Mo}_x\text{W}_{1-x}\text{O}_6$  microstructures with a tunable morphology and composition ( $x = 0, 0.21, 0.35, 0.65, \text{ and } 1$ ) via a simple solvothermal method. The incorporation of the Mo component leads to an effective reduction of the  $\text{Bi}_2\text{Mo}_x\text{W}_{1-x}\text{O}_6$  product, which therefore increases the utilization efficiency of visible light in water oxidization. The band-gap narrowing effect upon Mo incorporation is attributed to the creation of defect levels just below the CB, which is confirmed by DFT calculation results.  $\text{Bi}_2\text{Mo}_{0.21}\text{W}_{0.79}\text{O}_6$  PBMs were found to have the best activity in visible-light driven oxygen evolution from water splitting, and the enhanced photoactivity can be explained in terms of reduced band gap, as well as enhanced charge separation, due to optimized incorporation of Mo. This work presents a simple synthetic method for designing metal-incorporated semiconductors with porous structures for different applications.

## Acknowledgements

Financial support from the Natural Science Foundation of China (21171146 and 21371152), Zhejiang Provincial Natural Science Foundation of China (LR14B010001), the Zhejiang Provincial Public Welfare Project (2016C31015) and the State Key Laboratory of Silicon Materials at Zhejiang University (2015–10) is gratefully acknowledged.

## References

- S. S. K. Ma, T. Hisatomi, K. Maeda, Y. Moriya and K. Domen, *J. Am. Chem. Soc.*, 2012, **134**, 19993.
- F. Jiao and H. Frei, *Energy Environ. Sci.*, 2010, **3**, 1018.
- K. Maeda, D. L. Lu and K. Domen, *Angew. Chem., Int. Ed.*, 2013, **52**, 6488.
- K. Maeda, A. Xiong, T. Yoshinaga, T. Ikeda, N. Sakamoto, T. Hisatomi, M. Takashima, D. Lu, M. Kanehara, T. Setoyama, T. Teranishi and K. Domen, *Angew. Chem., Int. Ed.*, 2010, **122**, 4190.
- M. W. Kanan and D. G. Nocera, *Science*, 2008, **321**, 1072.
- M. R. Gao, Y. F. Xu, J. Jiang, Y. R. Zheng and S. H. Yu, *J. Am. Chem. Soc.*, 2012, **134**, 2930.
- J. Pfrommer, M. Lublow, A. Azarpira, C. Göbel, M. Lücke, A. Steigert, M. Pogrzeba, P. W. Menezes, A. Fischer, T. Schedel-Niedrig and M. Driess, *Angew. Chem., Int. Ed.*, 2014, **53**, 5183.
- G. G. Zhang, S. H. Zang and X. C. Wang, *ACS Catal.*, 2015, **5**, 941.
- G. S. Li, D. Q. Zhang, J. C. Yu and M. K. H. Leung, *Environ. Sci. Technol.*, 2010, **44**, 4276.
- F. Amano, A. Yamakata, K. Nogami, M. Osawa and B. Ohtani, *J. Am. Chem. Soc.*, 2008, **130**, 17650.
- N. Zhang, R. Ciriminna, M. Pagliaro and Y. J. Xu, *Chem. Soc. Rev.*, 2014, **43**, 5276.
- L. Korosi, S. Papp, I. Bertoti and I. Dekany, *Chem. Mater.*, 2007, **19**, 4811.
- M. Zhou, H. B. Wu, J. Bao, L. Liang, X. W. D. Lou and Y. Xie, *Angew. Chem., Int. Ed.*, 2013, **52**, 8579.
- Y. Peng, M. Yan, Q. G. Chen, C. M. Fan, H. Y. Zhou and A. W. Xu, *J. Mater. Chem. A*, 2014, **2**, 8517.
- Q. C. Xu, Y. H. Ng, Y. Zhang, J. S. C. Loo, R. Amal and T. T. Y. Tan, *Chem. Commun.*, 2011, **47**, 8641.
- W. J. Yang, B. Ma, W. C. Wang, Y. W. Wen, D. W. Zeng and B. Shan, *Phys. Chem. Chem. Phys.*, 2013, **15**, 19387.
- D. J. Wang, G. L. Xue, Y. Z. Zhen, F. Fu and D. S. Li, *J. Mater. Chem.*, 2012, **22**, 4751.
- J. Yang, X. H. Wang, Y. M. Chen, J. Dai and S. H. Sun, *RSC Adv.*, 2015, **5**, 9771.
- R. Shi, G. L. Huang, J. Lin and Y. F. Zhu, *J. Phys. Chem. C*, 2009, **113**, 19633.
- N. Tian, Y. H. Zhang, H. W. Huang, Y. He and Y. X. Guo, *J. Phys. Chem. C*, 2014, **118**, 15640.
- X. Ding, K. Zhao and L. Z. Zhang, *Environ. Sci. Technol.*, 2014, **48**, 5823.
- C. Bhattacharya, H. C. Lee and A. J. Bard, *J. Phys. Chem. C*, 2013, **117**, 9633.
- X. C. Song, Y. F. Zheng, R. Ma, Y. Y. Zhang and H. Y. Yin, *J. Hazard. Mater.*, 2011, **192**, 186.
- L. Zhou, M. M. Yu, J. Yang, Y. H. Wang and C. Z. Yu, *J. Phys. Chem. C*, 2010, **114**, 18812.
- R. Qiao, M. M. Mao, E. L. Hu, Y. J. Zhong, J. Q. Ning and Y. Hu, *Inorg. Chem.*, 2015, **54**, 9033.
- X. H. Gao, H. B. Wu, L. X. Zheng, Y. J. Zhong, Y. Hu and X. W. Lou, *Angew. Chem., Int. Ed.*, 2014, **53**, 5917.
- D. K. Ma, S. M. Huang, W. X. Chen, S. W. Hu, F. F. Shi and K. L. Fan, *J. Phys. Chem. C*, 2009, **113**, 4369.
- Y. Zhou, E. Antonova, Y. H. Lin, J. D. Grunwaldt, W. Bensch and G. R. Patzke, *Eur. J. Inorg. Chem.*, 2012, **5**, 783.
- H. G. Yu, Z. F. Zhu, J. H. Zhou, J. Wang, J. Q. Li and Y. L. Zhang, *Appl. Surf. Sci.*, 2013, **265**, 424–430.
- L. W. Zhang, H. B. Fu, C. Zhang and Y. F. Zhu, *J. Phys. Chem. C*, 2008, **112**, 3126.
- Y. G. Su, B. L. Zhu, K. Guan, S. S. Gao, L. Lv, C. F. Du, L. M. Peng, L. C. Hou and X. J. Wang, *J. Phys. Chem. C*, 2012, **116**, 18508.

- 32 F. D. Hardcastle and I. E. Wachs, *J. Raman Spectrosc.*, 1995, **26**, 397.
- 33 M. Crane, R. L. Frost, P. A. Williams and J. T. Kloprogge, *J. Raman Spectrosc.*, 2002, **33**, 62.
- 34 F. D. Hardcastle and I. E. Wachs, *J. Phys. Chem.*, 1991, **95**, 10763.
- 35 Y. F. Li, D. H. Xu, J. I. Oh, W. Z. Shen, X. Li and Y. Yu, *ACS Catal.*, 2012, **2**, 391–397.
- 36 Z. H. Sun, J. J. Guo, S. M. Zhu, L. Mao, J. Ma and D. Zhang, *Nanoscale*, 2014, **6**, 2186.
- 37 M. T. Greiner, M. G. Helander, W. M. Tang, Z. B. Wang, J. Qiu and Z. H. Lu, *Nat. Mater.*, 2012, **11**, 76.
- 38 X. K. Wang, Z. Q. Li, Z. W. Zhang, Q. Li, E. Y. Guo, C. X. Wang and L. W. Yin, *Nanoscale*, 2015, **7**, 3604.
- 39 D. Li, Y. D. Huang, N. Sharma, Z. X. Chen, D. Z. Jia and Z. P. Guo, *Phys. Chem. Chem. Phys.*, 2012, **14**, 3634.
- 40 N. Qiu, J. Zhang, Z. Y. Wu, T. D. Hu and P. Liu, *Cryst. Growth Des.*, 2012, **12**, 629.
- 41 T. Taniguchi, T. Watanabe, N. Sakamoto, N. Matsushita and M. Yoshimura, *Cryst. Growth Des.*, 2008, **8**, 3725.
- 42 S. C. Erwin, L. Zu, M. I. Haftel, A. L. Efros, T. A. Kennedy and D. J. Norris, *Nature*, 2005, **436**, 91–94.
- 43 G. Dalphian and J. A. Chelikowsky, *Phys. Rev. Lett.*, 2006, **96**, 226802.
- 44 M. Perez, *Scr. Mater.*, 2005, **52**, 709.
- 45 J. L. Hu, H. S. Qian, J. J. Li, Y. Hu, Z. Q. Li and S. H. Yu, *Part. Part. Syst. Charact.*, 2013, **30**, 306.
- 46 A. Kudo, I. Tsuji and H. Kato, *Chem. Commun.*, 2002, **73**, 1958.
- 47 Y. Zhou, Z. P. Tian, Z. Y. Zhao, Q. Liu, J. H. Kou, X. Y. Chen, J. Gao, S. C. Yan and Z. G. Zou, *ACS Appl. Mater. Interfaces*, 2011, **3**, 3594.
- 48 L. Zhang, Y. Man and Y. F. Zhu, *ACS Catal.*, 2011, **1**, 841.
- 49 R. M. Dreizler and E. K. Gross, *Density Functional Theory: an Approach to the Quantum Many-Body Problem*, Springer-Verlag, Berlin, 1990.
- 50 H. B. Fu, C. S. Pan, W. Q. Yao and Y. F. Zhu, *J. Phys. Chem. B*, 2005, **109**, 22432.
- 51 Y. F. Li, D. H. Xu, J. I. Oh, W. Z. Shen, X. Li and Y. Yu, *ACS Catal.*, 2012, **2**, 391.
- 52 X. Li, J. G. Yu, J. X. Low, Y. P. Fang, J. Xiao and X. B. Chen, *J. Mater. Chem. A*, 2015, **3**, 2485.
- 53 H. Li, F. Li, B. B. Zhang, X. Zhou, F. S. Yu and L. C. Sun, *J. Am. Chem. Soc.*, 2015, **137**, 4332.
- 54 Z. Li, C. Kong and G. X. Lu, *J. Phys. Chem. C*, 2016, **120**, 56.
- 55 R. L. Lee, P. D. Tran, S. S. Pramana, S. Y. Chiam, Y. Ren, S. Y. Meng, L. H. Wong and J. Barber, *Catal. Sci. Technol.*, 2013, **3**, 1694.
- 56 J. Ran, J. Zhang, J. G. Yu, M. Jaroniec and S. Z. Qiao, *Chem. Soc. Rev.*, 2014, **43**, 7787.
- 57 A. Etogo, E. Hu, C. M. Zhou, Y. J. Zhong, Y. Hu and Z. L. Hong, *J. Mater. Chem. A*, 2015, **3**, 22413.